Editors' Suggestion

# Balancing orbital effects and on-site Coulomb repulsion through Na modulations in $Na_xVO_2$

Xi Chen,* Hao Tang,* Yichao Wang, and Xin Li†
*John A. Paulson School of Engineering and Applied Sciences, Harvard University, Cambridge, Massachusetts 02138, USA*

(Received 21 December 2020; revised 29 June 2021; accepted 19 July 2021; published 6 August 2021)

Vanadium oxides have been highly attractive for over half a century since the discovery of the metal insulator transition near room temperature. Here $Na_xVO_2$ is studied through a systematic comparison with other layered sodium metal oxides with early 3*d* transition metals, first disclosing a unified evolution pattern of Na density waves through *in situ* x-ray diffraction analysis. Combining *ab initio* simulations and theoretical modelings, a sodium-modulated Peierls-like transition mechanism is then proposed for the bonding formation of metal ion dimers. More importantly, the unique trimer structure in $Na_xVO_2$ is shown to be very sensitive to the on-site Coulomb repulsion value, suggesting a delicate balance between strong electronic correlations and orbital effects that can be precisely modulated by both Na compositions and atomic stackings. This unveils a unique opportunity to design strongly correlated materials with tailored electronic transitions through electrochemical modulations and crystallographic designs, to elegantly balance various competition effects. We think the understanding will also help further elucidate complicated electronic behaviors in other vanadium oxide systems, as well as help improve electrochemical performances in layered metal oxides for Na ion battery applications.

DOI: 10.1103/PhysRevMaterials.5.084402

## I. INTRODUCTION

Vanadium oxide is one of the most widely studied prototypical strongly correlated materials. The discovery of the metal-insulator transition in $VO_2$ [1,2] triggers extensive research regarding its origin and potential technological impact for over half a century [3–14]. Goodenough [15] proposed a picture emphasizing the lattice and orbital effects, based on the single-particle theory of Peierls instability and the dimerization induced by the large crystal field splitting and hybridization gap. Later, Pouget *et al.* [16] and Zylbersztejn and Mott [17] emphasized the importance of electronic correlations to explain a new phase with alternating zigzag and dimerized chains by substituting only 0.2% of V in $VO_2$ by Cr [18]. Other theoretical models thus have been focused on either or both effects [19–22], to try to understand the relationship between the two in the vanadium system.

Recently, experimental studies of the layered $Na_xVO_2$ ($0 < x < 1$) revealed important phenomena closely related to $VO_2$ [23]. The layered $Na_{1/2}VO_2$ system was found to exhibit a magnetic phase transition concurrent with an insulator to metal transition at 322 K. Peculiar V trimers were also found to form at certain Na compositions, and *in situ* x-ray diffraction (XRD) measurements identified a Na composition region with a continuous shift of superstructure peaks. $NaVO_2$ in fact belongs to a general material category of layered sodium transition metal oxides, i.e., $NaTMO_2$ (TM: transition metal), where all the 3*d* TM types have been synthesized and electrochemically tested for changing Na compositions, partly driven by the strong interest in the field of sodium ion batteries. This freedom in the choice of transition metal elements with varying 3*d* electrons per TM ion is accompanied with the freedom in the electrochemical control of Na compositions through deintercalation, and the abundant interlayer stacking types and Na orderings, where the valence distribution and local environment of TM ions can be precisely tuned. These freedoms also make the material system a unique platform to fine-tune the electron correlations and orbital interactions with unprecedented precision and flexibility that other metal oxide systems cannot match.

In this paper, we study $Na_xVO_2$ through the systematic comparison with other $Na_xTMO_2$ (TM for early 3*d* transition metal of Ti, V, Cr). Specifically, we note that similar to $Na_xVO_2$, a continuous shift of XRD peaks with Na compositions was also observed in $Na_xTiO_2$ [24] and our own $Na_xCrO_2$ experiments here. We will first solve the Na ordering patterns from the *in situ* XRD, giving a unified evolution pattern in the form of Na density waves (NDWs). We then present a picture that reconciles strong electronic correlations and orbital effects in $Na_xTMO_2$ using combined approaches of *ab initio* DFT simulations and theoretical modeling. We propose a sodium-modulated Peierls-like transition mechanism for the bonding between TM dimers. More importantly, the unique trimer structure in $Na_xVO_2$ is shown to be a result of competition between the on-site Coulomb repulsion and orbital effects, which thus can be precisely modulated by a delicate collaboration of Na compositions and three-dimensional atomic stackings to switch on and off. Our findings unveil a unique opportunity to design strongly correlated materials with tailored electronic transitions through electrochemical modulations and crystallographic designs, to elegantly balance various competition effects. Moreover, the general Na density wave pattern shared by these many materials here may help understand unique Na diffusion and phase transition mechanisms in layered sodium transition metal oxides for Na ion battery applications.

*These authors contributed equally to this paper.
†lixin@seas.harvard.edu

 

## II. METHODS

*DFT.* The geometric optimization and electronic structures are calculated by the density functional theory (DFT) and projector-augmented wave pseudopotential implemented in the Vienna *ab initio* simulation package (VASP) code with an energy cutoff of 520 eV [25,26]. For the normal accuracy calculation, we use the generalized gradient approximation (GGA) of the Perdew-Burke-Ernzerhof (PBE) functional [27]. The on-site Coulomb repulsion is considered through GGA+$U$ methods with the default $U$ values of 0, 3.1, and 3.5 eV for Ti, V, and Cr, respectively, as reported in previous papers [28]. The energy converges to $10^{-5}$ eV for electronic iteration and the residue forces converge to 0.02 eV/Å for ionic relaxation. The Monkhorst package for $k$-point mesh is used with $k$-points separation of fewer than 0.04 $Å^{-1}$ [29]. The DFT-D3 methods are used for van der Waals correction [30,31]. Comparisons are made between results of GGA with different $U$ values and the $GW$ methods [32,33] for the $Na_xVO_2$ system to discuss the competition between bonding and on-site Coulomb repulsion. For $GW$ calculation, we first obtain a one-electron basis set from a standard DFT calculation and use the basis set for the self-consistent QPGW algorithm [33] as the second step, where both the eigenvalues and one-electron orbitals are updated. The charge differential densities are calculated by a three-step procedure. (1) Calculate the charge density $n_1(r)$ distribution of the structure with the NDW and dimers/trimers. (2) Fix certain TM atoms to the lattice sites of the dimer/trimer, and calculate the corresponding charge density $n_2(r)$ without forming the electronic dimer/trimer bondings. (3) Ensure that the considered atom(s) for both cases overlap, and calculate the charge density difference $n_1(r)$–$n_2(r)$. This function reflects the charge transfer during the formation of dimer/trimer bonds.

*One-dimensional and two-dimensional tight-binding models.* The origin of Na-modulated electronic interaction is analyzed by a tight-binding effective Hamiltonian model,

$$\hat{\mathrm{H}} = \sum_{i,\alpha} \epsilon_{i,\alpha} c^{+}_{i,\alpha} c_{i,\alpha} + \sum_{i,j,\alpha,\beta} t^{\alpha,\beta}_{i,j} c^{+}_{i,\alpha} c_{j,\beta} + U \sum_{i} n_{i\uparrow} n_{i\downarrow} + \frac{1}{2} m\omega^2 \sum_{i} x_i^2 + \frac{1}{2} \sum_{i,j} v_{ij} N_i N_j, \tag{1}$$

where $c^{(+)}$ denotes creation/annihilation operator of electrons, $n_{i\uparrow/\downarrow}$ represents electrons in TM $d$ orbitals, $N_i$ denotes Na occupation in the corresponding interstices, and $x$ is the displacement of transition metal ions. The orbital energy $\epsilon = -(e_0 N_0 + e_1 N_1)$ and hopping integral $t = t_0 + t_N N_t + t_d \Delta r$ are controlled by Na occupation, which gives rise to the Na-induced electronic effect. $N_0$ and $N_1$ are the numbers of sodium ions directly above a TM atom and at the direction that the bonding $d$ orbitals orient to, respectively. $N_t$ is the number of sodium ions that are adjacent to the O atom on the bonding route. $\Delta r$ is the distance between two TM ions after considering the displacement of TM ions. $e_0$, $e_1$, $t_N$, $t_d$, and $t_0$ are coefficients in the model and are set as constants as intrinsic properties of the systems. Their values are determined through the comparison with the orbital polarization and dimer bond length in the DFT calculations.

A one-dimensional (1D) chain model with $d_{xy}$ bonding orbitals and the nearest $\sigma$ interaction is used with second-order perturbation methods (regarding the deviation of Na distribution from the uniformity perturbation) to derive the Fermi level instability (see Supplemental Material [34]).

To simulate the dimer formation for specific materials, the nonperturbation calculation considering the discrete distribution of Na ions is implemented by solving the tight-binding model accurately. For each distribution of transition metal and sodium ions, we have a set of $\epsilon_i$ and $t_{i,i+1}$ coefficients and can solve the band structure by the corresponding electronic Hamiltonian $H_e$. The electron occupations $n$ are solved iteratively. Given a set of values for $n_l$ at step $l$, we use $n_l$ to obtain the value for on-site Coulomb repulsion energy and plug the value into Eq. (1) as a constant. We then solve for the band structure and obtain the new occupations $n_{l+1}$ by diagonalizing the tight-binding part of Eq. (1) including the first three terms. The value of the $U$ term we plugged in will contribute to the diagonal of the matrix for the Hamiltonian (i.e., it will add to the orbital energy $\epsilon_i$). Summing the band energy over the Brillouin zone gives the total electronic energy. Together with the harmonic potential and Coulomb repulsion, we have

$$E_{\mathrm{tot}} = 2S_{\mathrm{u.c.}} \sum_{n,\mathrm{occ}} \int_{\mathrm{BZ}} \frac{d^2\boldsymbol{k}}{(2\pi)^2} E_n(\boldsymbol{k}) + \frac{1}{2} m\omega^2 \sum_{\boldsymbol{i}} \boldsymbol{r}_{\boldsymbol{i}}^2 + \frac{1}{2} \sum_{\boldsymbol{i},\boldsymbol{j}} v_{\boldsymbol{ij}} N_{\boldsymbol{i}} N_{\mathbf{j}}, \tag{2}$$

where $S_{\mathrm{u.c.}}$ is the area of the unit cell. Ionic relaxation of TM ions is implemented by minimizing the above function numerically, and the electronic structures are calculated by the convergent atomic positions. The trend of displacement and fluctuation of orbital occupation for different materials is calculated through this procedure in Fig. 4(e).

The Hamiltonian of our two-dimensional (2D) model is

$$\hat{H}_{\mathrm{2D}} = \sum_{\boldsymbol{i},\alpha} (\epsilon_0 + \Delta\epsilon_{\boldsymbol{i},\alpha}) c^{+}_{\boldsymbol{i},\alpha} c_{\boldsymbol{i},\alpha} + \sum_{\boldsymbol{i},\alpha} \sum_{\boldsymbol{j}=\boldsymbol{i}\pm\boldsymbol{i}_\alpha} \left(t_0 + \Delta t^{\alpha}_{\boldsymbol{i},\boldsymbol{j}}\right) c^{+}_{\boldsymbol{i},\alpha} c_{\boldsymbol{j},\alpha} + \frac{1}{2} m\omega^2 \sum_{\boldsymbol{i}} \boldsymbol{r}_{\boldsymbol{i}}^2 + \frac{1}{2} \sum_{\boldsymbol{i},\boldsymbol{j}} v_{\boldsymbol{ij}} N_{\boldsymbol{i}} N_{\mathbf{j}}, \tag{3}$$

where $\boldsymbol{i} = (i_1, i_2)$ goes through all TM atoms; $\alpha$ goes through $d_{xy}$, $d_{yz}$, and $d_{xz}$ orbitals; and $\Delta\epsilon_{\boldsymbol{i},\alpha}$ and $\Delta t^{\alpha}_{\boldsymbol{i},\boldsymbol{j}}$ are determined by the Na environment as described in Eq. (1). It considers $t_{2g}$ orbitals (the first term) and $\sigma$ type hopping between them; they point directly to each other (the second term). The harmonic potential of the TM atoms and the Na Coulomb repulsion terms are just to replace the 1D coordinates by 2D vectors compared to the 1D model. Similar to the 1D case, atomic relaxation processes are used to consider the Na effect on the trimer formation, as briefly described by minimizing the total

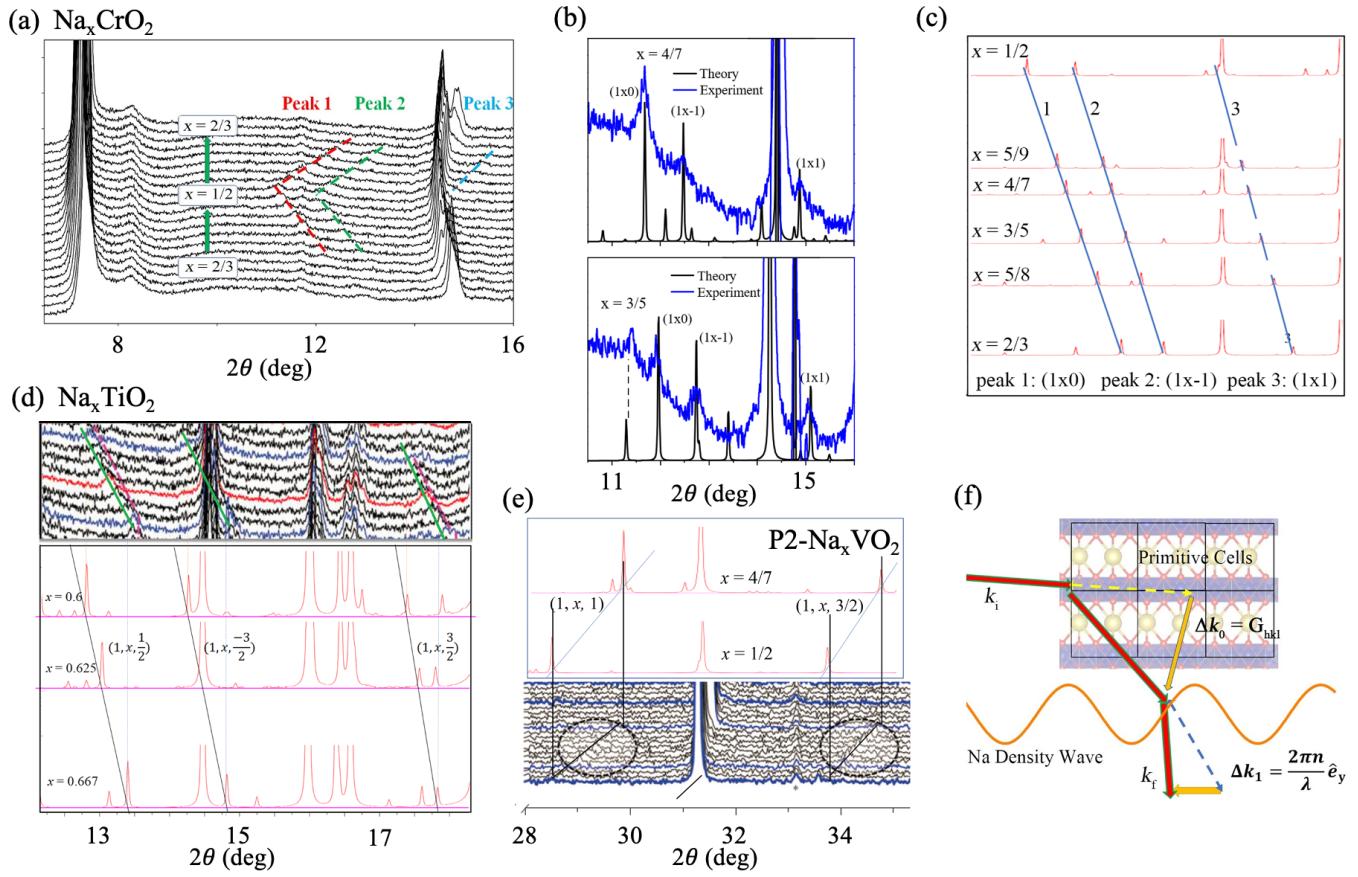


FIG. 1. (a) *In situ* XRD (Mo source) measurement of $Na_xCrO_2$ with three continuously moving superstructure peaks. The charging process of the *in situ* battery cell ends at $x = 1/2$. (b) Comparison of the *in situ* XRD (blue lines) and the spectra simulated from the solved superstructures (black lines) for two intermediate compositions $x = 4/7$ and 3/5 of $Na_xCrO_2$. The major and superstructure peaks are all consistent, confirming the solved structures. (c) Simulated superstructure XRD peak evolution of $Na_xCrO_2$ from our solved structures. (d) Superstructure evolution of $Na_xTiO_2$ from both the *in situ* XRD (Mo source) experiments and solved structure simulations. The *in situ* XRD data are from the previous work [24] where three peaks were observed. The solved Na orderings for $Na_xTiO_2$ are also fully supported by our *ex situ* synchrotron XRD analysis. (e) Superstructure evolution of $Na_xVO_2$ from both the *in situ* XRD (Cu source) experiments and solved structure simulations. The *in situ* XRD data are from the previous work [23]. (f) Illustration of the mechanism of how the XRD peak position continuously moves together with NDW wavelength during the (de-) intercalation process.

energy as follows:

$$\min_{\{r_i\}} E_{\text{tot}} = \min_{\{r_i\}} \left[ 2S_{\text{u.c.}} \sum_{n,\text{occ}} \int_{\text{BZ}} \frac{d^2\boldsymbol{k}}{(2\pi)^2} E_n(\{\boldsymbol{r_i}\}, \boldsymbol{k}) + \frac{1}{2} m\omega^2 \sum_i \boldsymbol{r}_i^2 + \frac{1}{2} \sum_{i,j} v_{ij} N_i N_j \right], \quad (4)$$

where $E_n(\{\boldsymbol{r_i}\}, \boldsymbol{k})$ is the electronic bands under the atomic configuration $\{\boldsymbol{r_i}\}$, $S_{\text{u.c.}}$ is the area of the unit cell. The first term (electronic energy) is integrated over the first Brillouin zone and summed over all occupied bands. On-site Coulomb repulsion $U$ was not applied in the 2D model, due to the complexity of the 2D quantum many-body problem, and because the model is sufficient without $U$ as we only use it to simulate and understand the effect from the specific Na environment that leads to trimer bonds in P2-$Na_xVO_2$, which agrees well with the DFT and experimental results. The different Na stackings in O3 and P2 type materials are analyzed to quantify their modulation on the electronic structures. The energy curve as a function of TM displacement is calculated to reveal the Na driving force to the dimer formation and the spontaneous symmetry-breaking process during the trimer formation.

*XRD*. The *in situ* lab XRD for $NaCrO_2$ was taken on a Bruker D8 X-ray diffractometer equipped with a Mo source from a homemade *in situ* electrochemical cell with a Be window. The $NaCrO_2$ sample was synthesized following previous works in the literature [35]. The *in situ* cell was charged galvanostatically at C/50 rate between 2.0 and 4.5 V on a Solartron 1287 with each XRD pattern scanned from a 6.5° to 30.5° $2\theta$ angle range (equivalent to 14.1°–69.7° on a Cu source) for 1 h, corresponding to 2% Na composition resolution per XRD pattern.

## III. RESULTS

### A. Na density wave in $Na_xTMO_2$

Recent *in situ* XRD experiments of $Na_xTMO_2$ (TM = Ti, V) clearly reveal the existence of incommensurate sodium orderings, with superstructure peak positions moving

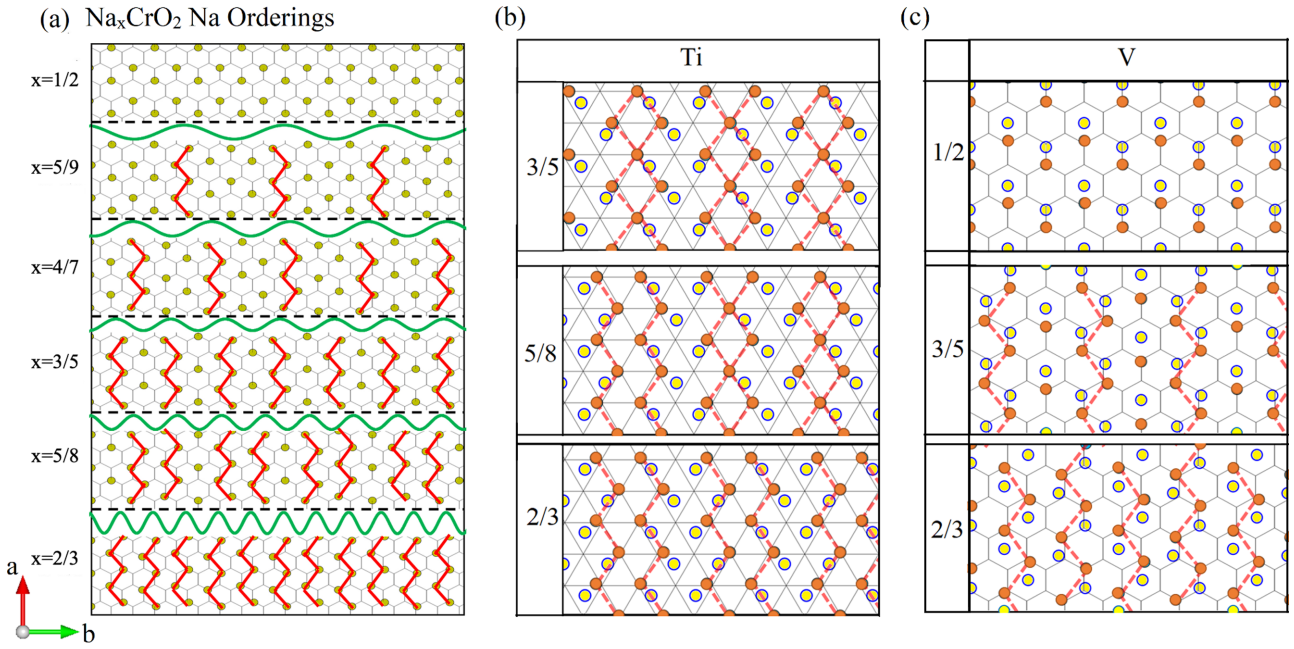


FIG. 2. Superstructure evolution and Na density wave (NDW) in $Na_xTMO_2$ (TM = Ti, V, Cr). (a) Superstructure evolution in $Na_xCrO_2$ for $x$ in (1/2, 2/3). The Na ions are denoted by yellow disks on the hexagonal lattices. Antiphase boundaries and NDW with continuously varying wavelengths are denoted by red zigzag lines and green wave patterns, respectively. (b) Superstructure evolution of $Na_xTiO_2$. (c) Superstructure evolution of $Na_xVO_2$. The yellow and orange disks denote Na ions from two neighboring Na layers in the corresponding two-layer supercells. The transition metal types and Na compositions are denoted on the top and left-hand sides of the figures, respectively. The stacking of Na along the transition metal layers is along the $c$ direction, following the O′3, P2, and P′3 types of oxygen stacking in the O′3-Ti, P2-V, and P′3-Cr, respectively. The notations of O′3, P2, and P′3 and the corresponding interlayer stackings are explained in Fig. S1 and Table S1 in the Supplemental Material [34].

continuously and quickly as a function of sodium composition $x$ [23,24]. This is analogous to the incommensurate electron or hole charge density waves found in other strongly correlated materials, including high-temperature cuprate superconductors [36]. Here we first present a systematic comparison of the phase evolution in $Na_xTMO_2$ with early $3d$ TM = Ti, V, Cr. The Na incommensurate orderings of $Na_xCrO_2$ corresponding to the *in situ* XRD patterns [Figs. 1(a)–1(c)] are solved, with representative patterns at several discrete Na compositions shown in Fig. 2(a). At $x = 2/3$, which is the starting point of the superstructure peaks in electrochemical charge, Na ions form "zigzag" stripes along the $a$ direction, similar to the antiphase boundary Na ordering patterns predicted in $Na_xCoO_2$ recently [37]. With further charging to $x < 2/3$, more and more such zigzag stripes are replaced by another type of low-density stripes, until the low-density stripe region fully takes over at $x = 1/2$.

Here we view the Na ordering patterns in $1/2 < x < 2/3$ as Na density waves (NDWs) with varying wavelengths. We find that similar NDW patterns [Figs. 2(b) and 2(c)] can also be identified from our analysis of previously reported *in situ* XRD results in $Na_xTMO_2$ with TM = Ti [Fig. 1(d)] [24] and V [Fig. 1(e)] [23]. The fast and continuous evolution of the superstructure XRD peaks with changing Na compositions compared with the largely static background major *hkl* peaks can be understood as a two-component scattering, illustrated by orange arrows in Fig. 1(f), with critical parameters listed in Table S1 in the Supplemental Material [34]. The consistency of the XRD patterns between experiments and simulations based on our solved structures is therefore illustrated in Fig. 1. These structures with NDW are generally not the electrostatic ground states, which suggests that electronic effects overcome the Coulomb repulsion between sodium ions to enable the formation of the Na density wave.

### B. Transition metal dimer coupled with NDW

DFT relaxations of the $Na_xTMO_2$ structures with the solved Na orderings identify the formation of TM dimers, with shortened TM-TM bonds. The TM dimers are found to have varying strengths with Na compositions and TM types, and are closely related to the NDW pattern. Figure 3(a) shows the DFT relaxed structure of $Na_{2/3}TiO_2$. We observed the slight displacement of the TM atoms away from the octahedral center and the formation of the TM dimers at the Na density peak area of the NDW. With the formation of dimer bonds, electrons transfer from the $d_{xz}$ and $d_{yz}$ orbitals of both Ti ions in a dimer to their $d_{xy}$ orbitals [Fig. 3(b)]. Since the $d_{xy}$ orbitals of the two bonding Ti ions point toward each other [Fig. 3(c)], it suggests that the dimers are bonded together in $\sigma$ bonds.

The origin of the orbital interaction is further analyzed from the electronic structures. The $d$ bands of transition metals in $Na_xTMO_2$ are separated to the $t_{2g}$ and $e_g^*$ bands. The Ti ions in $Na_xTiO_2$ have occupation levels within $t_{2g}$ orbitals, and similar for other early $3d$ transition metals such as V and Cr [38]. The projected density of states (PDOS) of the

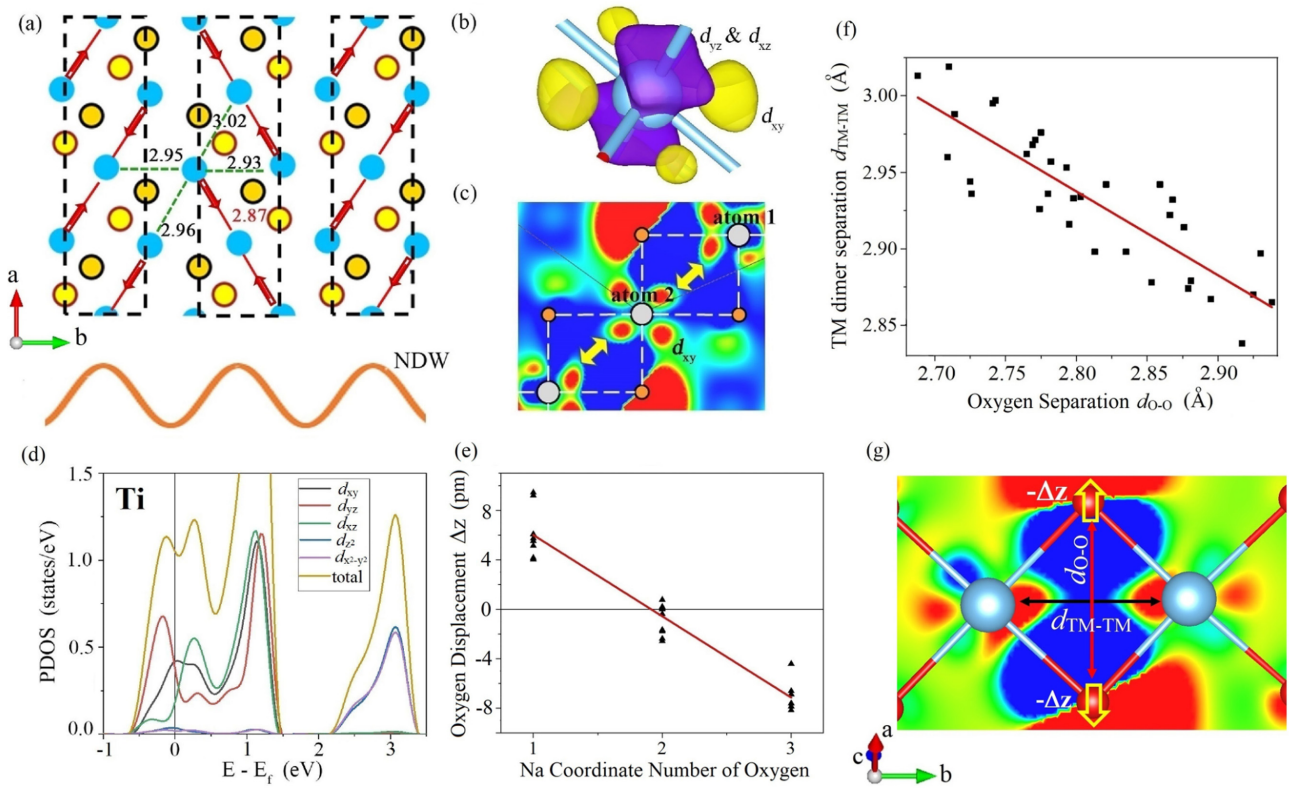


FIG. 3. Dimer and orbital interactions of NDW structures. (a) Na density wave and the corresponding bonds and charge density wave of $Na_{2/3}TiO_2$. The Ti ions in a specific layer are represented by the blue disks, and the Na ions above and below the $TiO_2$ layer are represented by the dark yellow and bright yellow disks, respectively. The labeled distances between the Ti atoms are in units of Å. (b) Positive and negative isosurface of charge density difference around Ti atoms. Electrons transfer from the purple $d_{yz}$ and $d_{xz}$ orbitals to the yellow $d_{xy}$ orbital. (c) Charge density difference between the NDW phase and the uniform phase without dimer (see Methods). Electrons are introduced to red areas which indicate $d_{xy}$ orbitals and $\sigma$ bonds. (d) PDOS of $Na_{0.6}TiO_2$ projected on the $d$ orbitals of an atom involved in a dimer. The states from about –0.5 to 1.5 eV are from $t_{2g}$ orbitals, while the states from about 2 to 3.5 eV are from $e_g^*$ orbitals. (e) Displacement of oxygen atoms in the $z$ direction vs the number of adjacent Na ions from statistics of a series of solved superstructures of $Na_xTiO_2$. Negative $\Delta z$ is the distortion toward the Na layer direction. (f) Relationship between the distance of the two oxygen atoms on different sides of the Ti ion layer and the corresponding TM dimer length. (g) Illustration of quantities defined in (e), (f).

$t_{2g}$ orbitals of the dimers, including the $d_{yz}$ and $d_{xz}$ orbitals for two different orientations, split into two peaks around the Fermi level as shown in Fig. 3(d), with the band below and above Fermi level as the bonding and antibonding states for TM dimers, respectively. For the polarized $d$ orbitals below the Fermi level, $d_{yz}$ shows higher occupation than $d_{xz}$ and $d_{xy}$, further suggesting the major contribution of the $d_{yz}$ orbital in the bonding state.

Importantly, we find that the dimer bonding formation is actually also modulated by local Na environments. The positively charged Na ions apply the negative local potential modulation for electrons in the $d_{xy}$ bonding orbitals, especially for those pointed directly to the Na ions (Fig. S2(a) [34]), resulting in a higher local electron density (Fig. S2(b) [34]). The modulation also pulls the negatively charged oxygen ions away from the Ti layer. These subtle crystal and electronic structural distortions further enhance the Ti-Ti bonding. The modulation effects are quantified based on the DFT simulations of such Na ordering supercells in Figs. 3(e) and 3(f). Our analysis shows the strong linear correlations between higher local Na ion density and larger oxygen displacement $-\Delta z$ away from the $TiO_2$ layer, and also the linear correlation between the separation of TM ions $d_{TM-TM}$, as a metric for the TM dimer strength, and that of oxygen ions $d_{O-O}$. These quantities are illustrated in Fig. 3(g).

Furthermore, such interactions show unique material dependency. Although $Na_xCrO_2$ shows an electronic structure similar to that of $Na_xTiO_2$ (Figs. S3(a) and 3(c) [34]), interestingly, O′3-$Na_{1/2}VO_2$ [39] and P2-$Na_{1/2}VO_2$ open band gaps at the Fermi level (Figs. S3(b) and 3(d) [34]), and display much stronger bonding interactions than the Ti and Cr systems.

### C. Sodium-modulated Peierls-like transition

Considering the quasi-1D nature of electronic localization discussed above, we start our modeling with the 1D chain tight-binding model shown in Fig. 4(a) to simulate the key mechanism of dimer formation by first considering the simplest case with the bonding interaction dominated by a single $d$ orbital. The model considers the following effective Hamiltonian, with the modulation of sodium environments on the orbital energy and tunneling coefficients between adjacent $d_{xy}$

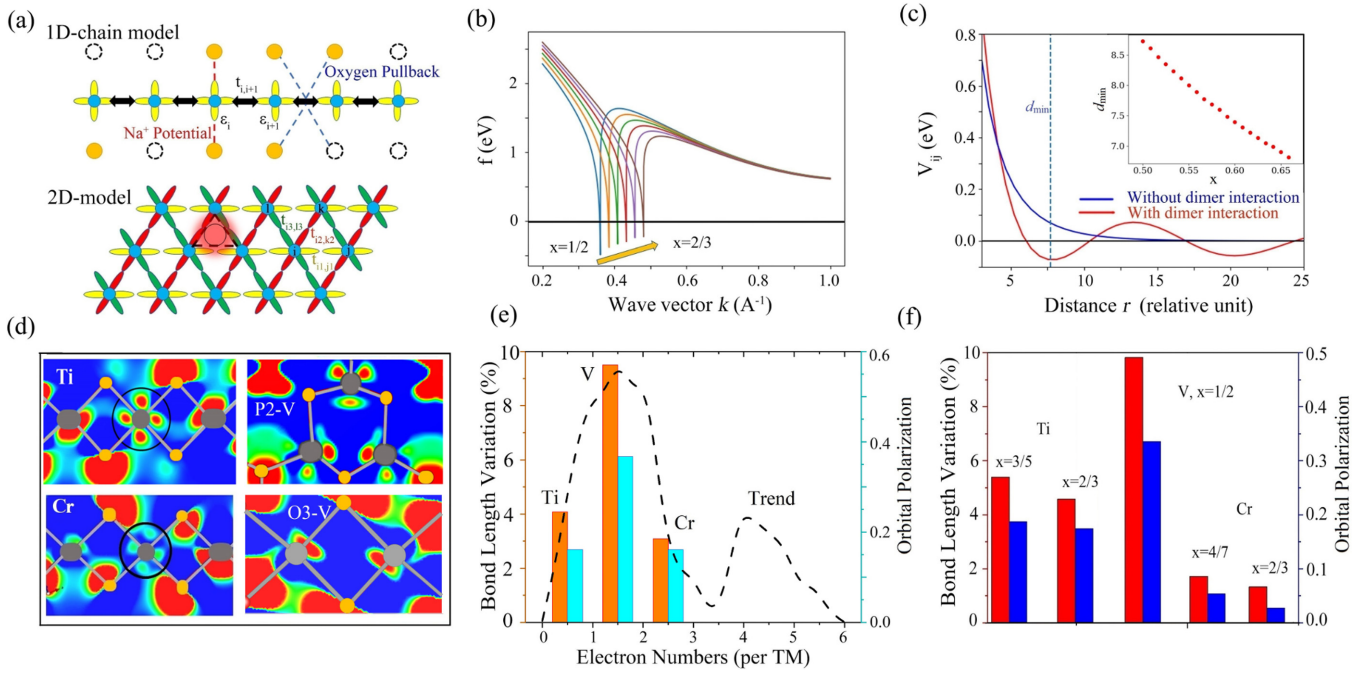


FIG. 4. Mechanism of the instability-induced dimer and material trend. (a) Illustration of the simplified 1D and 2D models. In the 1D model, a single $d_{xy}$ orbital (yellow lobes) is considered for each TM ion (green disks). The Na (yellow disks) distribution modulates both the illustrated orbital energy $\epsilon$ and the hopping integral $t$ of electrons. Empty circles indicate Na vacancies. In the 2D model, we consider the three $t_{2g}$ orbitals for each TM ion shown by yellow, green, and red lobes, respectively, as well as the hopping integrals between adjacent TM orbitals pointing to each other. (b) Energy coefficient $f_k$ of NDW formation in the wave vector space. (c) The effective potential of the interaction between Na ions at Na composition $x = 1/2$ given by the 1D model. The blue curve shows the screened Coulomb interaction (see Methods) between Na ions, while the red curve is given by our model with the electronic interaction added. The inset shows the continuous change of the Na-Na distance at the first minimum in the main plot with the Na composition $x$. (d) Charge introduced into $d_{xy}$ bonding orbitals for O′3-$Na_{2/3}TiO_2$, O′3-$Na_{1/2}VO_2$, P2-$Na_{1/2}VO_2$, and P′3 − $Na_{1/2}CrO_2$. Electrons transfer to the reddish area upon the formation of dimer or trimer bonds. (e) Tight-binding model simulated dimer displacement or bond length variation (brown), and the dimer-induced variation of electrons in bonding orbitals, i.e., orbital polarization (blue), for different materials. The dashed black line is the 1D model calculated trend with the continuous change of electron numbers. (f) Comparison between bonding length change and bonding order of the dimer bond formation, i.e., orbital polarization, for different TM and Na composition $x$ from DFT. The O′3-$Na_{1/2}VO_2$ is considered in (e), (f).

orbitals as identified by DFT,

$$\hat{H} = \sum_{i,\alpha} \epsilon_{i,\alpha} c^{+}_{i,\alpha} c_{i,\alpha} + \sum_{i,j,\alpha,\beta} t^{\alpha,\beta}_{i,j} c^{+}_{i,\alpha} c_{j,\beta} + U \sum_{i} n_{i\uparrow} n_{i\downarrow} + \frac{1}{2} m\omega^2 \sum_{i} x_i^2 + \frac{1}{2} \sum_{i,j} v_{ij} N_i N_j,$$

where $c^{(+)}$, $n_{i\uparrow/\downarrow}$, $N_i \in \{0, 1\}$, and $x$ represent the annihilation (creation) operator of electrons, electron number operator, Na occupation in the corresponding sites, and displacement of transition metal ions. The model includes orbital energy $\epsilon$, hopping integral $t$, on-site Coulomb repulsion $U$, harmonic potential for TM ions, and screened Na-Na repulsion $v_{ij}$ (see Supplemental Material [34]).

Our model first predicts NDW by describing it as an instability of the uniform Na distribution. By deriving the variation of total energy in response to the variation of Na density $n(k)$ in the momentum space, $\delta E[n] = 1/2 \sum_k f_k n(k)^2$, we find that negative coefficients $f_k$ emerge at a certain interval of $k$ [Fig 4(b)], indicating instability of the uniform Na distribution, because the formation of the NDW with the corresponding wave vector $k$ will decrease the energy of the system. Detailed derivation can be found in Methods. The most preferred NDW vector corresponds to the sharp valley in $f_k$ that moves continuously as a function of the Na composition $x$ [Fig. 4(b)]. The valley of potential occurs around 0.35–0.5 $Å^{-1}$, which roughly reflects the Na-Na distance that decreases from around 3 to 2 Å in real space as the Na composition increases from 1/2 to 2/3.

We then use our model to study the electronic and other ground-state properties by solving the tight-binding Hamiltonian at specific discrete Na distributions. The coupling between Na ions and $d_{xy}$ orbitals causes a Peierls-like transition, where the positions of TM ions in our model will be relaxed to form dimer bonds, and the effective interaction potential between Na ions at ground state shows several local minima [Fig. 4(c)] that continuously move with Na composition $x$ [Fig. 4(c), inset]. Such modified potential drives the ground-state Na ordering away from the electrostatic ground state, and the continuous evolution of local minima also corresponds to the continuous evolution of NDW upon (de-) intercalation of Na ions.

The strength of dimer bonds exhibits a trend for early 3$d$ TM = Ti, V, Cr [Fig. 4(d)]. The intensity of dimer-induced charge density is higher for Ti and V (red regions in the circled area) and lower for Cr, indicating that overdoping $t_{2g}$

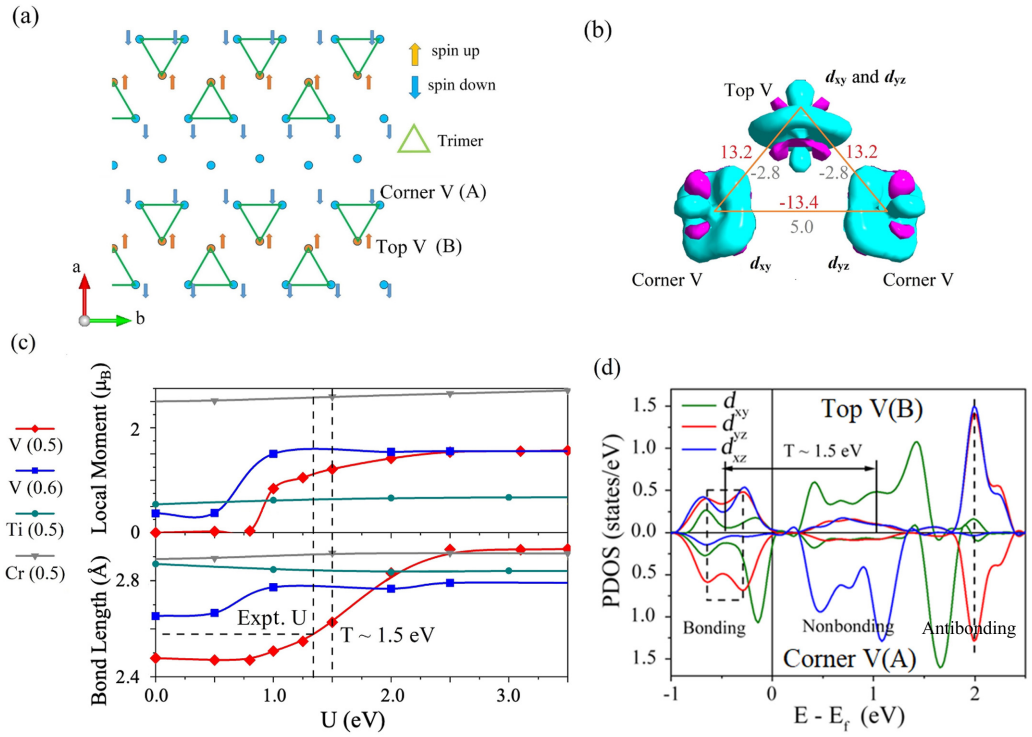


FIG. 5. Vanadium trimers of P2-$Na_{1/2}VO_2$. (a) Optimized structure of P2-$Na_{1/2}VO_2$ by the GGA functional ($U = 0$). Trimer bonds of V atoms exist with opposite local magnetic moments at corners (A) and top (B) sites. (b) Interorbital charge transfer and magnetic interaction $J$ in trimer bonds. Charge transfers from the blue area to the purple area. The gray and red digits represent the value of $J$ in units of eV for low $U$ (1.5 eV) and high $U$ (2.5 eV), respectively. Positive and negative values indicate ferromagnetic (FM) and antiferromagnetic (AFM) couplings, respectively. (c) Average magnetic moment on TM sites and dimer/trimer bond length as a function of Hubbard $U$ value for TM = O′3 − Ti, P2-V, and P′3-Cr at Na composition $x = 1/2$, as well as for P2-V at $x = 0.6$. (d) Projected DOS of P2-$Na_{1/2}VO_2$ calculated by the $GW$ method, projected to the top V ($B$) and Corner V ($A$) in the trimer. The bands are divided into bonding orbitals, nonbonding orbitals, and antibonding orbitals in the trimer bonds.

orbitals will limit the bonding capability and hence weaken the strength of dimer bonds. Furthermore, both $Na_xVO_2$ phases show the uniqueness of V in orbital structures. The strong dimer distortion in O3-$Na_{1/2}VO_2$ makes the shape of $d_{xy}$ orbitals almost unrecognizable, while special V trimer bonds appear with a cloverleaf pattern of bonding orbitals in P2-$Na_{1/2}VO_2$.

The effect is further quantified by the orbital polarization or bonding order, which we define as the dimer-induced variation of the electrons in bonding orbitals, and is technically calculated as the number of bonding electrons minus that of antibonding ones. Our tight-binding model predicts the TM dependency of bonding strength measured by the bond length variation and orbital polarization for $Na_xTMO_2$ [Fig. 4(e)], which well matches the DFT simulations [Fig. 4(f)].

### D. Uniqueness of $Na_xVO_2$ with $x$- and $U$-dependent trimers

The number of $d$ electrons, as the only variable in our model, plays a crucial role in the observed trend of the TM-TM coupling strength. The uniqueness for TM = V in Figs. 4(e) and 4(f) is also related to the filling levels of its $t_{2g}$ orbitals compared with other TM types. In Fig. S3 [34], the Fermi level for Ti is at the left DOS peak and the dimer interaction strongly splits the peak, while $E_f$ stays at the right peak for Cr, where such splitting effect due to dimer interaction is weak. In contrast, the $t_{2g}$ orbitals of TM = V are filled up to a valley in DOS, splitting out a small band gap and making the $t_{2g}$ orbitals very susceptible to polarization in the bonding and antibonding orbitals with large separations. A typical band structure calculated from our 1D model (Fig. S4 [34]) shows that the Fermi level of Ti falls in the lower-energy area of splitting, while the Cr falls to the higher-energy area, consistent with the DFT analysis.

The unique trimer bonds and bonding orbitals in P2-$Na_{1/2}VO_2$ [Fig. 4(d)] imply a special electronic origin with a certain 2D nature, compared with the more 1D zigzag dimers. The DFT calculated P2-$Na_{1/2}VO_2$ structure is shown in Fig. 5(a), with 3/4 vanadium ions forming trimers. Atoms at the top and corner of the trimers are relaxed to opposite spin polarization directions in the ground state, forming ferromagnetic (FM) stripes along the $b$ direction with the interstripe antiferromagnetic (AFM) coupling. Our trimer pattern is supported by previous XRD refinements of P2-$Na_{1/2}VO_2$, while our AFM ordering pattern here is consistent with the AFM type of ordering within $VO_2$ layers inferred from the magnetic susceptibility measurement [23]. Note that vanadium trimers are also observed in Li-excess $Li_xVO_2$ [40].

The electronic orbital interaction with the formation of the trimer is visualized through the charge transfer shown in Fig. 5(b). Electrons transfer to the $t_{2g}$ orbitals involved in the trimer bonds from other $d$ orbitals during the bonding forma-

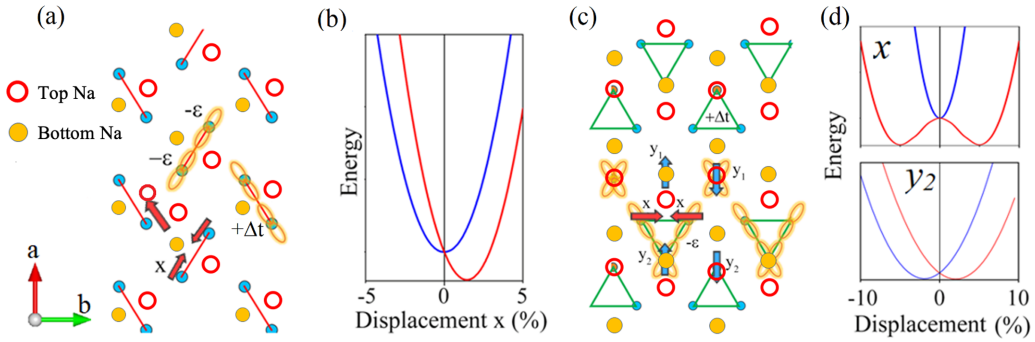


FIG. 6. Mechanism of trimer formation in P2-$Na_{1/2}VO_2$. (a) Na-coupled TM orbital interaction in O′3-$Na_{1/2}VO_2$ with the ground-state ionic dimers from our tight-binding models. The blue disks are V ions. The red circles and orange disks are Na ions on the top and bottom layers. (b) The local potential of the labeled ions in O′3-$Na_{1/2}VO_2$ along the local $x$ axis in (a). The red curve and blue curve describe the case with and without Na. (c) Ground-state ionic trimers in P2-$Na_{1/2}VO_2$ from our tight-binding models. The blue disks are V ions. The red circles and orange disks are Na ions in the top and bottom layers. (d) The local potential of the labeled ions in P2-$Na_{1/2}VO_2$ along the local $x$ and $y$ axes in (c). The red curve and blue curve describe the case with and without Na. Red and blue arrows in (a,c) indicate the displacement directions of several selected ions. Orange lobes illustrate the type of TM-TM bonding. $-\epsilon$ and $+\Delta t$ indicate the decrease of orbital energy and increase of the hopping integral induced by sodium. The results are consistent with our DFT simulations.

tion. The dominant bonding orbitals are the $d_{xy}$ and $d_{yz}$ ones of the corner V pointing to the top V, and the hybridization of the two corresponding $d$ orbitals of the top V atom [the purple ringlike orbital in Fig. 5(b)]. The localized bonding interaction therefore mainly appears between the top and corner atoms according to the orbital ordering in the trimer.

More interestingly, the bonding and trimer formation is also strongly correlated with the change of magnetic coupling, and both are controlled by the on-site Coulomb repulsion $U$ in our DFT simulations. At $U = 0$, spin orderings other than the one shown in Fig. 5(a) are all unstable in DFT, and all are relaxed to the ordering in Fig. 5(a). The trimer structure is maintained at $U = 1.5$ eV, where different spin orderings can be stabilized in DFT in order to compute the magnetic coupling $J$ based on the collinear model $E = \sum_{i,j} J_{ij}\sigma_i\sigma_j$. The solved magnitudes of $J$ [gray numbers in Fig. 5(b)] show the AFM coupling between the top and corner V atoms in the trimer, and the FM coupling between the two corner V atoms, which prefers the magnetic ordering in Fig. 5(a). On the contrary, at $U = 2.5$ the trimers disappear, and all the $J$ couplings flip the sign. The FM coupling between the top and corner V ions in the trimer and AFM coupling between the two corner V ions lead to an FM ordering for all the V ions, while the two corner V ions are thus frustrated considering their AFM $J$ coupling.

A systematic study of sweeping the $U$ value reveals that the structural and orbital sensitivity to the $U$ value only happens in the P2-$Na_xVO_2$ system near $x = 1/2$, indicating a unique mixture of structural, orbital, and strong electronic correlation effects. At $x = 1/2$, with $U$ value smaller than 0.8 eV, the strongest trimer bonds and the low net spin characterize the orbital-dominant condition with the electrons from the vanadium timers paired to form trimer bonds [Fig. 5(c)]. With $U > 1$ eV, the trimer bond length (between the top and corner atoms) and local magnetic moment gradually increase, indicating the gradual breaking of trimer bonds, until $U$ reaches approximately 2.5 eV. From the DOS calculation using the $GW$ method [Fig. 5(d)], which is in general considered to capture the strong electronic correlation more accurately, we identify that the average energy reduction of the bonding states is approximately 1.5 eV from the nonbonding states. Thus 1.5 eV becomes a critical value for the bonding energy of the trimer bonds to compete with the on-site Coulomb repulsion from the pair occupation in the bonding states, making the trimer bonds energetically sensitive to $U$ near the critical value.

By matching the trimer bond lengths from DFT and the experimental bond lengths at $x = 1/2$ [23] through sweeping $U$, we identify a value of $U_{\text{expt}} = 1.3$ eV that is slightly below the critical value of 1.5 eV. Therefore, it suggests that the experimental P2-$Na_{1/2}VO_2$ system slightly favors the bonding of the trimer over on-site Coulomb repulsion. More importantly, the recipient of $U_{\text{expt}}$ to the critical $U$ value makes the trimer susceptible to external perturbations. It is also important to note that the critical $U$ value also decreases with increasing Na composition in P2-$Na_xVO_2$ at $x > 0.5$, as demonstrated at $x = 0.6$ [Fig. 5(c)] suggesting the weakened bonding strength with Na doping that is consistent with the longer V-V bond length in the trimer [Fig. 5(c), bottom]. At higher Na composition at $x = 0.67$, such trimer completely disappears at any $U$ values.

To further reveal the mechanism of the trimer bonding and the uniqueness of V trimers in P2-$Na_{1/2}VO_2$, we first compare P2-$Na_{1/2}VO_2$ with O′3-$Na_{1/2}VO_2$. The comparison of orbital effects in dimer and trimer bonds is shown in Fig. 6. The energy curve as a function of displacement $x$ and $y_2$ (all other degrees of freedom are optimized) shows that the O3 dimer bonds [41] are a Na-induced drifting force, while the P2 trimer bonds exhibit spontaneous breaking of inversion symmetry, leading to "dimers" in the crystal $b$ direction. The difference originates from the different interlayer stackings of Na [Figs. 6(a) and 6(c)] as understood by our two-dimensional tight-binding model described in Fig. 4(a). In the O3 stacking system, the bonding strength of the dimer bonds denoted by red lines is enhanced by both the Na potential and the oxygen pullback effect, leading to lower orbital energy $\epsilon$ and stronger hopping integral $t$, as illustrated in Fig. 6(a). We can see that for every V dimer, the third V that forms a triangle with the

dimer is pulled away from the dimer, causing no formation of the trimer. On the contrary, the Na effects in P2-$Na_{1/2}VO_2$ enhance the electronic bonding between the corner and top V atoms and lead to trimer bonds. This is also true for Na composition $x$ at 0.6 that we checked in DFT simulations, where local Na environments close to P2-$Na_{1/2}VO_2$ still exist in the low-density area of the NDW in P2-$Na_{0.6}VO_2$.

In order for the trimer bonds to form among the three V ions, electrons from the top V ion need to overcome the on-site repulsion to occupy the three bonding orbitals. These orbitals are already half filled by the electrons from the two corner V atoms with down spins [Fig. 5(a)]. With the formation of the trimer, up spins are injected to the bonding orbital, which matches the observation of the disappearing local magnetic moment at $U_{expt}$ [Fig. 5(c), top] and the "singlet" state proposed for the V trimer in Li-excess $Li_xVO_2$ [40]. In contrast, the dimer bonds in these systems are insensitive to the $U$ value because no such extra pair occupation can be formed during the bonding process. Thus, the unique sensitivity to on-site Coulomb repulsion only exists for the trimer formation in P2-$Na_xVO_2$, where the competition between orbital and strong electronic correlation effects is balanced close to the critical value through Na modulations. More implicit modulation mechanisms, often applied through external parameters equivalent to the Na one here, are likely to play similar roles in modulating complicated electronic behaviors in other more controversial vanadium oxide systems.

## IV. CONCLUSION

We studied the vanadium oxide system through the perspective of Na modulations in a unique model system of layered $Na_xVO_2$. Through a systematic comparison with other $Na_xTMO_2$ (TM for early 3$d$ transition metal of Ti, V, Cr), we observed a similar continuous shift of XRD peaks with Na compositions, and we solved a unified evolution pattern in the form of Na density waves (NDWs). We proposed a sodium-modulated Peierls-like transition mechanism for the bonding between TM dimers for all three TM species. Specifically for $Na_xVO_2$, we articulate quantitatively that the metal insulator transition in P2-$Na_xVO_2$ is a result of delicate balances between competitive on-site Coulomb repulsion and orbital effects, which can be precisely modulated to switch on and off by alkaline ion compositions and three-dimensional atomic stackings. Our findings unveil a unique opportunity to design strongly correlated materials with tailored electronic transitions through electrochemical modulations, to elegantly balance various competition effects. We believe our understanding will also help further elucidate complicated electronic behaviors in other vanadium oxide systems, as well as help understand the related electrochemical performances for Na ion battery applications.

## ACKNOWLEDGMENTS

This work was supported by Dean's Competitive Fund for Promising Scholarship at FAS at Harvard University, and Harvard Data Science Initiative Competitive Research Award. Computations were supported by computational resources from the Extreme Science and Engineering Discovery Environment (XSEDE) and the Odyssey cluster supported by the FAS Division of Science, Research Computing Group at Harvard University. Use of the Advanced Photon Source at Argonne National Laboratory was supported by the U.S. Department of Energy, Office of Science, Office of Basic Energy Sciences, under Contract No. DE-AC02- 06CH11357.

[1] F. J. Morin, Oxides Which Show a Metal-to-Insulator Transition at the Néel Temperature, Phys. Rev. Lett. **3**, 34 (1959).
[2] W. Paul, The present position of theory and experiment for $VO_2$, Mater. Res. Bull. **5**, 691 (1970).
[3] O. A. Cook and O. A. Cook, High-temperature heat contents of $V_2O_3$, $V_2O_4$ and $V_2O_5$, J. Am. Chem. Soc. **69**, 331 (1947).
[4] R. M. Wentzcovitch, W. W. Schulz, and P. B. Allen, $VO_2$: Peierls or Mott-Hubbard? A View from Band Theory, Phys. Rev. Lett. **72**, 3389 (1994).
[5] M. A. Kats, R. Blanchard, S. Zhang, P. Genevet, C. Ko, S. Ramanathan, and F. Capasso, Vanadium Dioxide as a Natural Disordered Metamaterial: Perfect Thermal Emission and Large Broadband Negative Differential Thermal Emittance, Phys. Rev. X **3**, 041004 (2014).
[6] S. Cueff, D. Li, Y. Zhou, F. J. Wong, J. A. Kurvits, S. Ramanathan, and R. Zia, Dynamic control of light emission faster than the lifetime limit using $VO_2$ phase-change, Nat. Commun. **6**, 8636 (2015).
[7] V. Eyert, The metal-insulator transitions of $VO_2$: A band theoretical approach, Ann. Phys. **11**, 650 (2002).
[8] S. Biermann, A. Poteryaev, A. I. Lichtenstein, and A. Georges, Dynamical Singlets and Correlation-Assisted Peierls Transition in $VO_2$, Phys. Rev. Lett. **94**, 026404 (2005).
[9] A. Liebsch, H. Ishida, and G. Bihlmayer, Coulomb correlations and orbital polarization in the metal-insulator transition of $VO_2$, Phys. Rev. B **71**, 085109 (2005).
[10] R. Eguchi, M. Taguchi, M. Matsunami, K. Horiba, K. Yamamoto, Y. Ishida, A. Chainani, Y. Takata, M. Yabashi, D. Miwa, Y. Nishino, K. Tamasaku, T. Ishikawa, Y. Senba, H. Ohashi, Y. Muraoka, Z. Hiroi, and S. Shin, Photoemission evidence for a Mott-Hubbard metal-insulator transition in $VO_2$, Phys. Rev. B **78**, 075115 (2008).
[11] E. Strelcov, Y. Lilach, and A. Kolmakov, Gas sensor based on metal-insulator transition in $VO_2$ nanowire thermistor, Nano Lett. **9**, 2322 (2009).
[12] Z. Yang, C. Ko, and S. Ramanathan, Oxide electronics utilizing ultrafast metal-insulator transitions, Annu. Rev. Mater. Res. **41**, 337 (2011).
[13] V. Eyert, $VO_2$: A Novel View from Band Theory, Phys. Rev. Lett. **107**, 016401 (2011).
[14] Y. Gao, H. Luo, Z. Zhang, L. Kang, Z. Chen, J. Du, M. Kanehira, and C. Cao, Nanoceramic $VO_2$ thermochromic smart glass: A review on progress in solution processing, Nano Energy **1**, 221 (2012).
[15] J. B. Goodenough, The Two components of the crystallographic transition in $VO_2$, J. Solid State Chem. **3**, 490 (1971).

[16] J. P. Pouget, H. Launois, T. M. Rice, P. Dernier, A. Gossard, G. Villeneuve, and P. Hagenmuller, Dimerization of a linear Heisenberg chain in the insulating phases of $V_{1-x}Cr_xO_2$, Phys. Rev. B **10**, 1801 (1974).

[17] A. Zylbersztejn and N. F. Mott, Metal-insulator transition in vanadium dioxide, Phys. Rev. B **11**, 4383 (1975).

[18] M. Marezio, D. B. McWhan, J. P. Remeika, and P. D. Dernier, Structural aspects of the metal-insulator transitions in Cr-doped $VO_2$, Phys. Rev. B **5**, 2541 (1972).

[19] F. Grandi, A. Amaricci, and M. Fabrizio, Unraveling the Mott-Peierls intrigue in vanadium dioxide, Phys. Rev. Res. **2**, 013298 (2020).

[20] A. M. de Graff and R. Luzzi, Crystallographic distortion, electron-electron interaction, and the metal-nonmetal transition, Helv. Phys. Acta **41**, 764 (1968).

[21] D. Paquet and P. Leroux-Hugon, Electron correlations and electron-lattice interactions in the metal-insulator, ferroelastic transition in $VO_2$: A thermodynamical study, Phys. Rev. B **22**, 5284 (1980).

[22] J. Shi, R. Bruinsma, and A. R. Bishop, Theory of vanadium dioxide, Synth. Met. **43**, 3527 (1991).

[23] M. Guignard, C. Didier, J. Darriet, P. Bordet, E. Elkaïm, and C. Delmas, P2-$Na_xVO_2$ system as electrodes for batteries and electron-correlated materials, Nat. Mater. **12**, 74 (2013).

[24] D. Wu, X. Li, B. Xu, N. Twu, L. Liu, and G. Ceder, $NaTiO_2$: a layered anode material for sodium-ion batteries, Energy Environ. Sci. **8**, 195 (2015).

[25] G. Kresse and J. Furthmüller, Efficient iterative schemes for *ab initio* total-energy calculations using a plane-wave basis set, Phys. Rev. B **54**, 11169 (1996).

[26] D. Joubert, From ultrasoft pseudopotentials to the projector augmented-wave method, Phys. Rev. B **59**, 1758 (1999).

[27] J. P. Perdew, Burke, and Ernzerhof, Generalized Gradient Approximation Made Simple, Phys. Rev. Lett. **77**, 3865 (1996).

[28] G. Hautier, S. P. Ong, A. Jain, C. J. Moore, and G. Ceder, Accuracy of density functional theory in predicting formation energies of ternary oxides from binary oxides and its implication on phase stability, Phys. Rev. B **85**, 155208 (2012).

[29] D. J. Chadi, Special points for Brillouin-zone integrations, Phys. Rev. B **16**, 1746 (1977).

[30] S. Grimme, J. Antony, S. Ehrlich, and H. Krieg, A consistent and accurate *ab initio* parametrization of density functional dispersion correction (DFT-D) for the 94 elements H-Pu. J. Chem. Phys. **132**, 154104 (2010).

[31] S. Grimme, S. Ehrlich, and L. Goerigk, Effect of the damping function in dispersion corrected density functional theory, J. Comput. Chem. **32**, 1456 (2011).

[32] M. Shishkin and G. Kresse, Implementation and performance of the frequency-dependent *GW* method within the PAW framework, Phys. Rev. B **74**, 035101 (2006).

[33] M. Shishkin, M. Marsman, and G. Kresse, Accurate Quasiparticle Spectra from Self-Consistent *GW* Calculations with Vertex Corrections, Phys. Rev. Lett. **99**, 246403 (2007).

[34] See Supplemental Material at http://link.aps.org/supplemental/10.1103/PhysRevMaterials.5.084402 for detailed derivation and more supporting figures.

[35] S. H. Bo, X. Li, A. J. Toumar, and G. Ceder, Layered-to-rock-salt transformation in desodiated $Na_xCrO_2$ ($x$ 0.4), Chem. Mater. **28**, 1419 (2016).

[36] H. Miao, R. Fumagalli, M. Rossi, J. Lorenzana, G. Seibold, F. Yakhou-Harris, K. Kummer, N. B. Brookes, G. D. Gu, L. Braicovich, G. Ghiringhelli, and M. P. M. Dean, Formation of Incommensurate Charge Density Waves in Cuprates, Phys. Rev. X **9**, 031042 (2019).

[37] J. L. Kaufman and A. Van der Ven, $Na_xCoO_2$ phase stability and hierarchical orderings in the O3/P3 structure family, Phys. Rev. Mater. **3**, 15402 (2019).

[38] X. Li, Y. Wang, D. Wu, L. Liu, S. H. Bo, and G. Ceder, Jahn-Teller assisted Na diffusion for high performance Na ion batteries, Chem. Mater. **28**, 6575 (2016).

[39] C. Didier, M. Guignard, M. R. Suchomel, D. Carlier, J. Darriet, and C. Delmas, Thermally and electrochemically driven topotactical transformations in sodium layered oxides $Na_xVO_2$, Chem. Mater. **28**, 1462 (2016).

[40] F. Pourpoint, X. Hua, D. S. Middlemiss, P. Adamson, D. Wang, P. G. Bruce, and C. P. Grey, New insights into the crystal and electronic structures of $Li_{1+x}V_{1-x}O_2$ from solid state NMR, pair distribution function analyses, and first principles calculations, Chem. Mater. **24**, 2880 (2012).

[41] C. Didier, M. Guignard, J. Darriet, and C. Delmas, O3-$Na_xVO_2$ system: A superstructure for $Na_{1/2}VO_2$, Inorg. Chem. **51**, 11007 (2012).